Electron interferometry and quantum spin Hall phase in silicene

Bartłomiej Rzeszotarski, Alina Mreńca-Kolasińska, and Bartłomiej Szafran

AGH University of Science and Technology, Faculty of Physics and Applied Computer Science, al. Mickiewicza 30, 30-059 Kraków, Poland

We discuss devices for detection of the topological insulator phase based on the two-path electron interference. For that purpose we consider buckled silicene, for which a local energy gap can be opened by a vertical electric field to close one of the interference paths and for which the quantum spin Hall insulator conditions are controlled by the Fermi energy. In quantum spin Hall phase the interference is absent due to the separation of the spin currents, and the conductance of the devices include sharp features related to localized resonances. In the normal transport conditions the two-path interference produces regular Aharonov-Bohm oscillations in the external magnetic field.

I. INTRODUCTION

Silicene [1–3], the two-dimensional material that forms a honeycomb structure (similar to graphene), has recently been strongly examined regarding its synthesis [4]. Significant interest in this material mainly comes from two factors: (i) the strong intrinsic spin-orbit coupling [1,2] that accompanies the buckling and provides a wide variety of potential implementations in spintronics [5–8] as well as topological spintronics [9], and (ii) the potential of integration with currently well-known silicon technology [10]. Topological spintronics is a promising field where the electronic devices based on topological insulators will generate less heat and achieve higher performance [11] in comparison to silicon-semiconductor electronics.

Quantum spin Hall (QSH) insulators [12–14] form a class of two-dimensional topological insulators with bulk energy gap and topologically protected currents of a fixed spin-orbital helicity. The QSH phase [15] is discussed for bulk nanostructures including HgTe quantum wells [16–19] and InAs/GaSb interfaces [20,21]. In two-dimensional materials it has been investigated for bilayer graphene with spin-orbit coupling [22], twisted bilayer graphene [23,24], as well as graphenelike monolayer Xenes materials [25,26], including silicene [1–4,27]. The QSH conditions in silicene occur for Fermi energies near the charge neutrality point [1–4,27]. The Fermi energy in 2D monolayer materials can be controlled by external gating. In the QSH phase the spin currents are confined by opposite edges of the sample, which was used for proposals of spin sources and spin filters in silicene [5–8,28,29].

In this paper we propose electron interferometer devices that can be used for detection of the QSH transport conditions. The devices are based on the idea of two-path interference and the spin separation by the split silicene ribbon [5]. We consider a double-slit interference device as well as a quantum ring and find that in the normal phase one observes smooth Aharonov-Bohm conductance oscillations, while in the QSH regime only sharp conductance features due to the localized resonances with circular current loops are observed. In

silicene both the localized resonances and the Aharonov-Bohm oscillations can be intentionally switched off by applying a local electric field to one of the arms of the split channels, due to the buckling of the crystal lattice that translates the electric field into a local energy gap [30,31] that stops the current flow.

II. THEORY

A. Hamiltonian

We use the tight-binding Hamiltonian spanned on p_z orbitals of Si atoms [3]:

$$
\begin{aligned}
H = & -t \sum_{\langle i,j \rangle \alpha} c_{i\alpha}^\dagger c_{j\alpha} + i \frac{\lambda_{\mathrm{SO}}}{3\sqrt{3}} \sum_{\langle\langle i,j \rangle\rangle \alpha,\beta} \nu_{ij} c_{i\alpha}^\dagger \sigma_{\alpha,\beta}^z c_{j\beta} \\
& - i \frac{2}{3} \lambda_R^{\mathrm{int.}} \sum_{\langle\langle i,j \rangle\rangle \alpha,\beta} \mu_{ij} c_{i\alpha}^\dagger (\vec{\sigma} \times \vec{d}_{ij})_{\alpha\beta}^z c_{j\beta} \\
& + \sum_{i\alpha} V_{zi} c_{i\alpha}^\dagger c_{i\alpha},
\end{aligned}
\tag{1}
$$

where $c_{i\alpha}^\dagger$ ($c_{j\alpha}$) is the creation (annihilation) operator for an electron on atom i with spin α. The calculation accounts for a hexagonal lattice of Si atoms with constant $a = 3.89\,\text{Å}$ and a vertical shift of 0.46 Å between the A and B sublattices. Summations over $\langle i,j \rangle$ and $\langle\langle i,j \rangle\rangle$ run over nearest- and next-nearest-neighbor ions, respectively. In Eq. (1) we use $t = 1.6$ eV for the hopping energy [1,3], $\lambda_{\mathrm{SO}} = 3.9$ meV [3] is the intrinsic spin-orbit coupling energy [15], where $\nu_{ij} = -1$ (+1) for the clockwise (counterclockwise) next-nearest neighbor hopping, and $\lambda_R^{\mathrm{int.}} = 0.7$ meV is the intrinsic spin-orbit coupling energy [1,3], where the unit vector from the jth to ith ion $\mathbf{d}_{ij} = \frac{\mathbf{r}_j - \mathbf{r}_i}{|\mathbf{r}_j - \mathbf{r}_i|}$. Within sublattice A (B) we apply $\mu_{ij} = +1$ (−1). The last term in Eq. (2) introduces a local vertical electric field (yellow gates in Fig. 1) at the entrance to the slits to intentionally switch off the currents in the channels. The gates introduce a vertical electric field of about 100 mV/Å that produces the potential difference ±25 meV at the A and B sublattices of the buckled silicene lattice. The

(a)

(b)
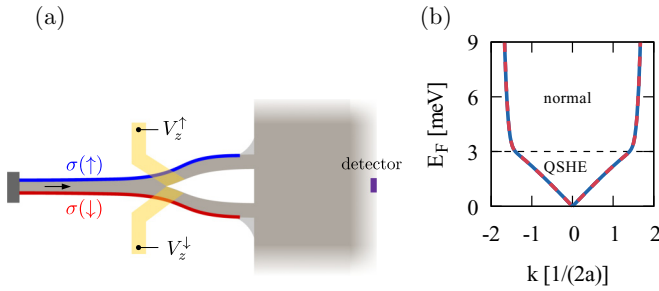
FIG. 1. (a) Sketch of the split-channel system. The input lead and the split channels are silicene ribbons of width 6.5 nm and zigzag edges. In the quantum spin Hall effect (QSHE) phase, each channel is fed by a different spin-state current from the input lead (the blue and red lines at the edges of the channel). The length of the split part is about 60 nm, and the vertical spacing between the split channels is 7 nm. The horizontal distance between openings of the slits and the detector is 32 nm. The detector is a ribbon 6.5 nm wide. External gates marked in yellow can be used to locally open the energy gap in silicene. (b) The spin-degenerate dispersion relation of the zigzag 6.5-nm-wide silicene ribbon at the conduction band side. The linear energy range corresponds to the QSH insulator phase. For higher E_F the spin for both spin orientations flows through the center of the ribbon.

field opens the local energy gap for the Fermi energy range considered here and closes the channel for the electron flow.

In the presence of an external perpendicular magnetic field B_z, the Peierls phase is introduced to the hopping terms $\mathbf{h}_{i\alpha j\beta}$ for the Hamiltonian, written in general form

$$H' = \sum_{i,j,\alpha,\beta} \mathbf{h}_{i\alpha j\beta} \exp\left[\frac{2\pi i}{\Phi_0} \int_{\mathbf{r}_i}^{\mathbf{r}_j} \mathbf{A} \cdot \mathbf{dl}\right] c_{i\alpha}^\dagger c_{j\beta}, \quad (2)$$

where $\mathbf{A}$ is the vector potential, $\Phi_0 = h/e$ is the magnetic flux quantum, and $\mathbf{r}_i$ is the position of the ith ion.

B. Method

In our calculations we use the wave-function matching (WFM) technique as described in Refs. [29,32]. The transmission probability from the input lead to mode k (output lead) is

$$T^k = \sum_l |t^{kl}|^2, \quad (3)$$

where t^{kl} is the probability amplitude for the transmission from mode l in the input lead to mode k in the output lead. For the mth mode with the wave function ψ^m, we distinguish spin by calculating $\langle \mathbf{S}_\bullet \rangle = \langle \psi^m | \sigma_\bullet | \psi^m \rangle$ as a quantum expectation value of the Pauli matrix through each atom inside the lead. The positive (negative) $\langle \mathbf{S}_\bullet \rangle$ values are labeled by u, $\uparrow$ (d, $\downarrow$). In this notation the spin-dependent conductance can be written as

$$G_{\mathfrak{ab}} = G_0 \sum_{k,l} |t^{kl}|^2 \delta_{\mathfrak{a},\alpha(l)} \delta_{\mathfrak{b},\beta(k)}, \quad (4)$$

where $G_0 = e^2/h$, and $\mathfrak{a}$ ($\mathfrak{b}$) is expected input (output) orientation of the spin, while α and β correspond to the signs of $\langle \mathbf{S}_\bullet \rangle$ value for a given mode. For example the

spin-conserving up-oriented conductance is calculated as $G_{uu} = G_0 \sum_{k,l} |t^{kl}|^2 \delta_{u,\alpha(l)} \delta_{u,\beta(k)}$ for $\langle \mathbf{S}_z \rangle = \langle \psi^m | \sigma_z | \psi^m \rangle$. All other components of the spin-dependent conductance can be calculated in the same manner.

In the tight-binding model the current flowing between i and j ions along the π bonds is calculated as

$$J_{i\alpha j\beta} = \frac{i}{h} \sum_{\alpha,\beta} [\mathbf{h}_{i\alpha j\beta} \Psi_{i,\alpha}^* \Psi_{j,\beta} - \mathbf{h}_{j\beta i\alpha} \Psi_{j,\beta}^* \Psi_{i,\alpha}], \quad (5)$$

where $\Psi_{j,\beta}$ is the β spin component of the wave function at the jth ion. Due to spin-orbit coupling included in Hamiltonian (1), the formula (5) also describes the currents that flow between different spin components.

III. RESULTS

A. Double-slit system

The schematics of the double-slit interferometer are depicted in [Fig. 1(a)]. The electrons are fed from the left by the silicene ribbon of a zigzag edge of 6.5 nm width. The zigzag ribbon supports the spin-polarized edge transport at the Fermi energy $E_F \in (-3, 3)$ meV with respect to the charge neutrality point [see the dispersion relation in Fig. 1(b)]. In the quantum spin Hall insulator phase the opposite spin currents flow at the opposite edges of the ribbon [see Fig. 1(a)]. The input lead splits into two channels of the same width. In the topological phase this spindle-shaped connection separates the opposite spin currents to the two channels [Fig. 1(a)].

The split channels are connected to a semi-infinite open plane of silicene [Fig. 1(a)] with smoothed extensions that prevent backscattering. At open half plane, the areas marked
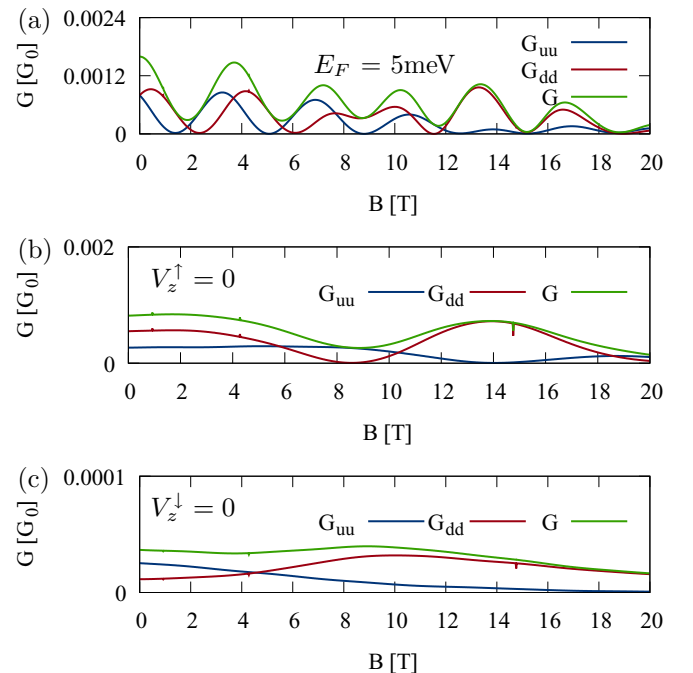
FIG. 2. Conductance with both channels (a), the upper (b) and lower (c) channel open for $E_F = 5$ meV (outside the QSHE regime). In (b) [(c)] the 100 meV/Å vertical electric field is applied to the lower [upper] channel.
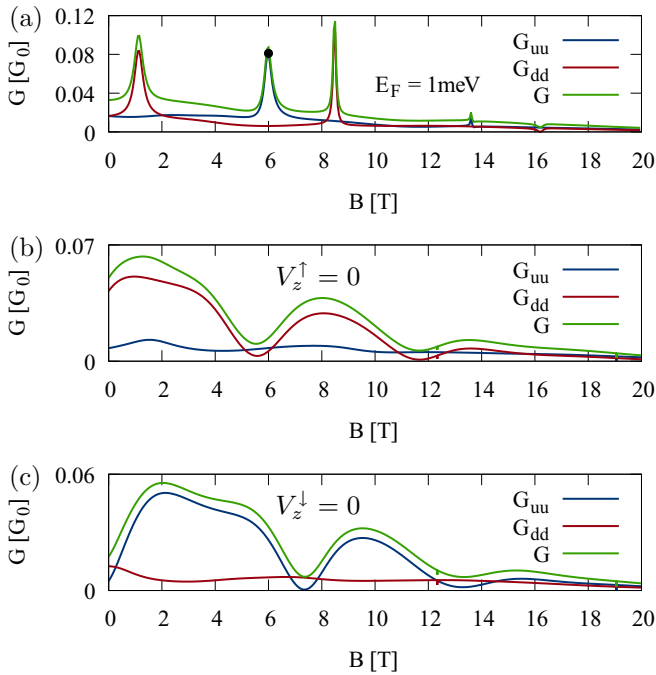
FIG. 3. (a) Two-slit interference for $E_F = 1$ meV (in the QSHE regime) in comparison to the one-slit transmissions (b, c). In (b) the upper slit is open ($V_z^\uparrow = 0$ and $V_z^\downarrow = 100$ meV/Å), while in (c) the lower slit is open ($V_z^\uparrow = 100$ meV/Å and $V_z^\downarrow = 0$).

by the gray color fading to white in Fig. 1(a), we attach wide silicene ribbons that make the edges of the computational box reflectionless. For $E_F > 3$ meV [Fig. 1(b)] the current flows through the bulk of the channel for both spin orientations, and we refer to these conditions as the normal phase. In the normal phase the current flows through both split channels for both spin orientations. The Young interference of the waves entering the open half plane by different slits can only occur in the normal phase. In the topological phase each of the slits feeds opposite spin. Thus, observation of the Young interference should depend on the Fermi energy. In order to
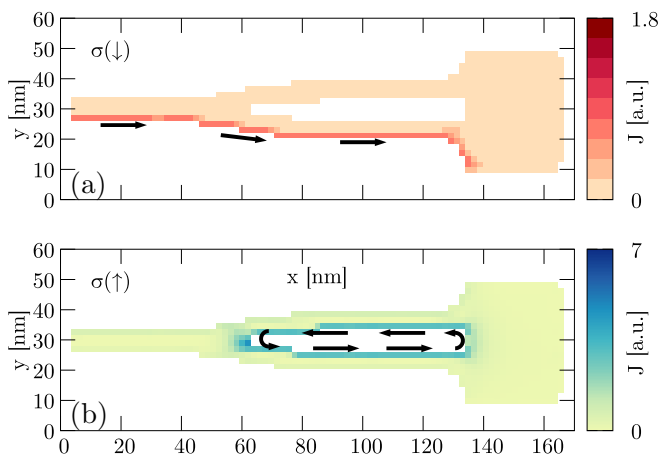
FIG. 4. The current map for $E_F = 1$ meV and $B = 6$ T [marked by dot in Fig. 3(c)]. Subplot (a) is for mode k_i associated with spin down [$\sigma(\downarrow)$] and (b) is for the spin up [$\sigma(\uparrow)$].
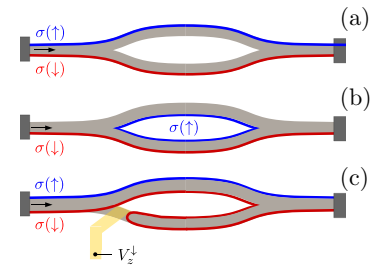
FIG. 5. Sketch of the quantum ring formed by reflection of the fork channel of Fig. 1. The current distributions observed in the QSH phase are given for off-resonant (a) and resonant (b) conditions and for the entrance of the lower lead closed by a local electrostatic potential.

monitor the interference in the model device [Fig. 1], at 32 nm to the right of the slit opening a zigzag ribbon of width 6.5 nm is connected as a detector [33]. In order to gain additional control in the interference device, we introduce local gates (yellow gates in Fig. 1) to switch off the currents.

Figure 2(a) shows the conductance in the absence of the electric field in the gated area in the normal phase for $E_F = 5$ meV. The conductance for both spin orientations and the total conductance undergo periodic oscillations in the external magnetic field with a period of about 4 T, which is the Aharonov-Bohm period for the area of about 1000 nm^2 enclosed between the electron paths passing through the split channels to the detector. For the lower [Fig. 2(b)] or upper [Fig. 2(c)] channel cut off by the vertical electric field, the Aharonov-Bohm conductance oscillations disappear, which is a signature of the switched-off two-slit interference.

In the QSH phase [Fig. 3(a)] we do not observe the regular AB oscillations, even for both channels open. The wave function for each spin passes through a single slit to the half plane so no Young interference can occur. Instead, in Fig. 3(a) we find sharp peaks of conductance which correspond to
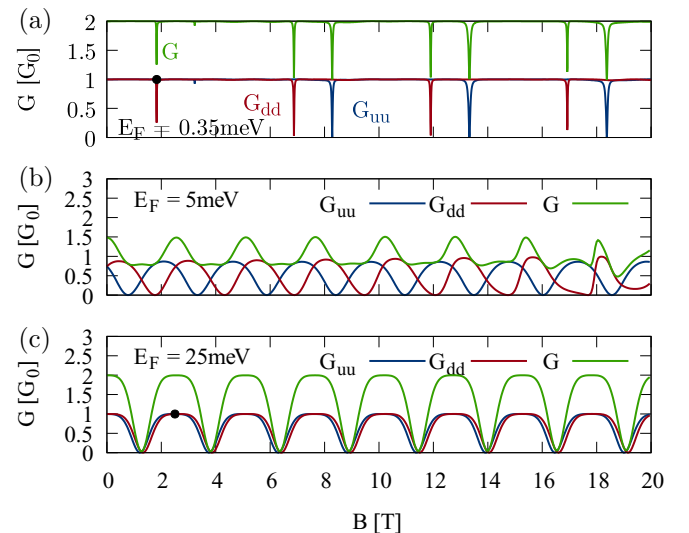
FIG. 6. Conductance of the quantum ring in the (a) QSH regime $E_F = 0.35$ meV and in the normal conditions for $E_F = 5$ meV (b) and 25 meV (c) in the absence of vertical electric field.

(a) $E_F = 0.35$ meV

(b) $E_F = 5$ meV
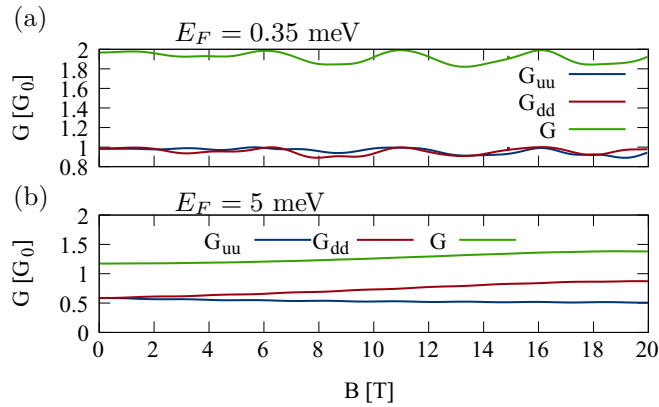
FIG. 7. (a, b) Same as Figs. 6(a) and 6(b) but in the presence of the local electric field in the entrance to the lower lead [Fig. 5(c)].

localized resonances with the current circulation around the etched area [see Fig. 4(b) for the point marked by the dot in Fig. 3(a)]. The local electric field which cuts off the upper or lower channels excludes the current circulation, and the rapid features of the conductance dependence on the external field disappear [Figs. 3(b) and 3(c)]. For one of the closed channels [Figs. 3(b) and 3(c)] the dominant spin in the detector is somewhat counterintuitive: when the lower channel—preferred by the spin-down currents—is closed, the calculated G_{dd} is much larger than G_{uu} [Fig. 3(b)] for a general B. The reason for this is that for $V_z^\downarrow \neq 0$ the spin-down current is directed to the upper channel where it flows near its lower edge and thus is closer to the detector.

B. Ring geometry

Similar control of the two-path interference effects can be obtained in a quantum ring [Fig. 5] formed by reflection of the split channel of Fig. 1(a). The calculated conductance in the QSH regime is given in Fig. 6(a) for $E_F = 0.35$ meV. For a general magnetic field the system is transparent for the electron flow [Fig. 5(a)]. Sharp dips of conductance appear [Fig. 6(a)] by interference with the localized loops of current stabilized near the inner edge of the ring [Fig. 5(b)]. Note that in the open system the conductance peaked by interference with localized states, because the signal received by the detector came from leakage [Fig. 3(a)] of the resonant current loop. The localized resonances are only weakly coupled to

the leads, hence their long lifetime, which is translated to narrow resonance widths. Under normal transport conditions [Figs. 6(b) and 6(c)], no sharp resonances appear and smooth AB oscillations appear with the period independent of the energy. For higher energy [Fig. 6(c)] the contribution of opposite spins to conductance becomes equal.

For the gate that cuts off the current flow across the lower channel [Fig. 5(c)], the dips due to the localized states disappear in the QSH regime [Fig. 7(a)] and the AB oscillations are removed in the normal conditions [Fig. 7(b)]. For the normal conditions at $B = 0$, the closed lower channel reduces the conductance significantly. In the QSH conditions, both spin currents find their way to the exit of the ring, although the path for the spin-down current becomes quite complex [Fig. 5(c)].

IV. SUMMARY

We have demonstrated that gated interference devices can be defined in silicene to allow for detection of the quantum spin Hall transport conditions by reaction of the conductance to the local electric fields closing one of the paths for the electron flow.

Considering double-slit geometry, the topological transport can be distinguished by sharp peaks in conductance—without any oscillations—in dependence of increasing external magnetic field amplitude. Conductance peaks are caused by localized resonances that occur as current flow around etched area. However, the normal transport is characterized by smooth Aharonov-Bohm oscillations.

In the system with ring geometry, the topological state is observed by sharp dips in conductance (in contrast to peaks in double slit), but the explanation of an effect remains the same, as well as for the normal transport recognition with Aharonov-Bohm oscillations.

[1] M. Ezawa, Phys. Rev. Lett. **109**, 055502 (2012); M. Ezawa, E. Salomon, P. De Padova, D. Solonenko, P. Vogt, M. E. Dávila, A. Molle, T. Angot, and G. Le Lay, Riv. Nuovo Cimento **41**, 175 (2018).

[2] C.-C. Liu, W. Feng, and Y. Yao, Phys. Rev. Lett. **107**, 076802 (2011).

[3] C.-C. Liu, H. Jiang, and Y. Yao, Phys. Rev. B **84**, 195430 (2011).

[4] A. Molle, C. Grazianetti, L. Tao, D. Taneja, M. H. Alam, and D. Akiwande, Chem. Soc. Rev. **47**, 6370 (2018).

[5] W.-F. Tsai, C.-Y. Huang, T.-R. Chang, H. Lin, H.-T. Jeng, and A. Bansil, Nat. Commun. **4**, 1500 (2013).

[6] X. Q. Wu and H. Meng, J. Appl. Phys. **117**, 203903 (2015).

[7] N. Missault, P. Vasilopoulos, V. Vargiamidis, F. M. Peeters, and B. Van Duppen, Phys. Rev. B **92**, 195423 (2015).

[8] K. Shakouri, H. Simchi, M. Esmaeilzadeh, H. Mazidabadi, and F. M. Peeters, Phys. Rev. B **92**, 035413 (2015).

[9] W. Luo, L. Sheng, B. G. Wang, and D. Y. Xing, Sci. Rep. **6**, 31325 (2016).

[10] S. Chowdhury and D. Jana, Rep. Prog. Phys. **79**, 126501 (2016).

[11] N. H. D. Khang, Y. Ueda, and P. N. Hai, Nat. Mater. **17**, 808 (2018).

[12] M. Z. Hasan and C. L. Kane, Rev. Mod. Phys. **82**, 3045 (2010).

[13] J. H. Bardarson and J. E. Moore, Rep. Prog. Phys. **76**, 056501 (2013).

[14] X.-L. Qi and S.-C. Zhang, Rev. Mod. Phys. **83**, 1057 (2011).

[15] C. L. Kane and E. J. Mele, Phys. Rev. Lett. **95**, 226801 (2005); **95**, 146802 (2005).

[16] B. A. Bernevig, T. L. Hughes, and S.-C. Zhang, Science **314**, 1757 (2006).

[17] M. König, S. Wiedemann, C. Brüne, A. Roth, H. Buhmann, L. W. Molenkamp, X.-L. Qi, and S.-C. Zhang, Science **318**, 766 (2007).

[18] A. Roth, C. Brüne, H. Buhmann, L. W. Molenkamp, J. Maciejko, X.-L. Qi, and S. C. Zhang, Science **325**, 294 (2009).

[19] C. Brüne, A. Roth, H. Buhmann, E. M. Hankiewicz, L. W. Molenkamp, J. Maciejko, X.-L. Qi, and S.-C. Zhang, Nat. Phys. **8**, 485 (2012).

[20] C. Liu, T. L. Hughes, X.-L. Qi, K. Wang, and S.-C. Zhang, Phys. Rev. Lett. **100**, 236601 (2008).

[21] I. Knez, R.-R. Du, and G. Sullivan, Phys. Rev. Lett. **107**, 136603 (2011).

[22] E. Prada, P. San-Jose, L. Brey, and H. A. Fertig, Solid State Commun. **151**, 1075 (2011).

[23] J. D. Sanchez-Yamagishi, J. Y. Luo, A. F. Young, B. M. Hunt, K. Watanabe, T. Taniguchi, R. C. Ashoori, and P. Jarillo-Herrero, Nat. Nanotechnol. **12**, 118 (2017).

[24] F. Finocchiaro, F. Guinea, and P. San-Jose, 2D Mater. **4**, 025027 (2017).

[25] A. Molle, J. Goldberger, M. Houssa, Y. Xu, S.-C. Zhang, and D. Akinwande, Nat. Mater. **16**, 163 (2017).

[26] Z. Liu, C.-X. Liu, Y. S. Wu, W. H. Duan, F. Liu, and J. Wu, Phys. Rev. Lett. **107**, 136805 (2011).

[27] E. Scalise, M. Houssa, E. Cinquanta, C. Grazianetti, B. van den Broek, G. Pourtois, A. Stesmans, M. Fanciulli, and A. Molle, 2D Mater. **1**, 011010 (2014).

[28] C. Nunez, F. Domínguez-Adame, P. A. Orellana, L. Rosales, and R. A. Römer, 2D Mater. **3**, 025006 (2016).

[29] B. Rzeszotarski and B. Szafran, Phys. Rev. B **98**, 075417 (2018).

[30] N. D. Drummond, V. Zólyomi, and V. I. Fal'ko, Phys. Rev. B **85**, 075423 (2012).

[31] Z. Ni, Q. Liu, K. Tang, J. Zheng, J. Zhou, R. Qin, Z. Gao, D. Yu, and J. Lu, Nano Lett. **12**, 113 (2011).

[32] K. Kolasiński, B. Szafran, B. Brun, and H. Sellier, Phys. Rev. B **94**, 075301 (2016).

[33] P. Khatua, B. Bansal, and D. Shahar, Phys. Rev. Lett. **112**, 010403 (2014).